MATERIALS CHEMISTRY FRONTIERS

CHINESE CHEMICAL SOCIETY

ROYAL SOCIETY OF CHEMISTRY

RESEARCH ARTICLE

View Article Online
View Journal | View Issue

Cite this: *Mater. Chem. Front.*, 2021, **5**, 5689

Asymmetric small organic molecule-based NIR-II fluorophores for high performance tumor phototheranostics†

Qi Wang, ‡[ab] Xinrui Niu,‡[a] Linqiang Yang,‡[c] Jiawei Liu,[a] Jing Wang,[a] Xingpeng Xu,[a] Weihua Tang, *[c] Wei Huang[a] and Quli Fan *[a]

Received 25th March 2021,
Accepted 26th May 2021

DOI: 10.1039/d1qm00472g

rsc.li/frontiers-materials

Small organic molecules hold great promise for phototheranostics due to their well-defined chemical structures and optical properties, excellent biodegradation and biocompatibility, high purity, and outstanding repeatability. Nevertheless, numerous small molecules exhibited weak absorption in the near-infrared I (NIR-I) region (particularly 808 nm, the optimal tissue transparent window in the NIR-I region), expedient NIR-I fluorescence emission, and single-mode therapy, which greatly hinder their phototheranostic performances. Herein, versatile nanoparticle DTPT NPs based on a single-component asymmetric small organic molecule were successfully constructed as a proof-of-concept example for high-performance phototheranostics. The developed DTPT NPs possessed strong absorption at 808 nm, excellent near-infrared II (NIR-II) fluorescence emission, prominent reactive oxygen species, and hyperthermia production ability (photothermal conversion efficiency was as high as 61.6%). Furthermore, upon a single 808 nm laser irradiation, the tumor inhibition rate of the versatile DTPT NPs was demonstrated to be 90.8%, profiting from the satisfactory NIR-II fluorescence imaging and photothermal/photodynamic performances. Moreover, the NPs showed superb safety to normal tissues, further demonstrating the potential application of NPs in clinical practice. This study provides an idea to construct small molecule-based nanoplatforms for high performance phototheranostics.

Introduction

Despite making considerable and significant advances to optimize the therapeutic outcomes, malignant tumors remain a grave threat to human health.[1] Recently, phototheranostics have been manifested as a non-invasive and effective medical technology to offer diverse information about cancer treatments such as real-time identification of tumor location and evaluation of therapeutic outcome, exhibiting huge advantages over conventional tumor therapeutics.[2] Unfortunately, the developed phototheranostic nanoplatforms are still hindered by multiple limitations: (1) they are generally constructed by integrating various diagnostic and therapeutic components, which results in complicated preparation routes and unstable nanostructures;[3] (2) multiple excitation wavelengths are usually needed to realize the functions of imaging and therapy, which may prolong therapy time and produce unjustified side effects to sufferers;[4] (3) the current phototheranostic systems mainly employ near-infrared I (NIR-I, 650–900 nm) fluorescence imaging.[5] However, its limited tissue penetration depth and spatial resolution tremendously hamper the diagnostic accuracy;[6] (4) most photothermal agents or photosensitizers are found to suffer from low photothermal conversion efficiency (PCE) or unsatisfactory reactive oxygen species (ROS) generation, which is harmful to photothermal therapy (PTT) or photodynamic therapy (PDT);[7] (5) single-mode PTT or PDT shows limited therapeutic efficacy.[8] Consequently, the exploration of single-component-based phototheranostic nanoplatforms for high performance diagnosis and therapy under single NIR illumination is extremely worthwhile.

It is well known that photons emitted from fluorophores exhibit higher tissue penetration depth, and less tissue scattering and absorption as wavelengths increase.[9] Near-infrared II (NIR-II, 1000–1700 nm) fluorescence imaging is skillfully devised for deep tissue diagnosis in recent years, which presents tremendous

[a] *State Key Laboratory of Organic Electronics and Information Displays & Jiangsu Key Laboratory for Biosensors, Institute of Advanced Materials (IAM), Jiangsu National Synergetic Innovation Center for Advanced Materials (SICAM), Nanjing University of Posts & Telecommunications, Nanjing 210023, China. E-mail: iamqlfan@njupt.edu.cn*

[b] *State Key Laboratory of Bioelectronics, Southeast University, Nanjing 210096, China*

[c] *School of Chemical Engineering, Nanjing University of Science and Technology, Nanjing 210094, China. E-mail: whtang@njust.edu.cn*

† Electronic supplementary information (ESI) available: Synthetic procedures, molar absorption coefficient *etc.* See DOI: 10.1039/d1qm00472g

‡ These authors contributed equally to this work.

advantages over NIR-I fluorescence imaging, such as high detection depth, ultralow auto-fluorescence, remarkable signal-to-background ratios, and superior image quality.[10] Till date, numerous inorganic nanomaterials[11] (*e.g.*, quantum dots and rare earth-doped nanoagents) and organic nanomaterials[12] (*e.g.*, conjugated polymers and small molecules) were constructed as NIR-II fluorophores. However, the clinical translation of inorganic nanomaterials was hampered by their potential toxicity concerns.[13] Moreover, conjugated polymers also have some defects, although they exhibit good biocompatibility. For instance, the molecular weights and optical properties may differ from batch to batch due to the challenging synthesis and purification processes.[14] In contrast, small organic molecules have well-defined chemical structures and optical properties, excellent biodegradation and biocompatibility, high purity, and outstanding repeatability.[15] Nevertheless, the excitation wavelengths of numerous small molecule-based NIR-II fluorophores were below 808 nm (optimal tissue transparent window in the NIR-I region).[16] Moreover, many small molecules only possess photothermal or photodynamic effects with low PCE value or ROS generation,[7e,17] which hinder their phototheranostic outcome. It was remarkable that the integration of PTT and PDT could effectively promote therapeutic performance by covering respective drawbacks.[18] Moreover, small molecules with asymmetric structures could effectively enhance intramolecular charge transfer,[19] leading to the amplification of photothermal conversion capability,[20] which is beneficial for tumor treatments. Moreover, according to the Jablonski diagram, the molecular structures of the organic phototheranostic agents significantly influence their optical performances.[21]

Based on the above-mentioned issues, herein, an asymmetric small organic molecule (DTPT) with proper electron acceptor and donor structures was developed as a proof-of-concept example for high performance phototheranostics (Scheme 1). To assure outstanding water-solubility and biocompatibility, DTPT was encapsulated by Pluronic F127 *via* one-step nanoprecipitation, obtaining DTPT nanoparticles (NPs). The resultant DTPT NPs possessed strong absorption at 808 nm, excellent NIR-II fluorescence emission, robust photostability, and high ROS and hyperthermia production ability (PCE was as high as 61.6%). The results from *in vitro* and *in vivo* assays affirmed that DTPT NPs displayed significant antitumor efficacy under a single 808 nm laser irradiation, profiting from the satisfactory NIR-II fluorescence imaging and PTT/PDT performances. Moreover, inappreciable harm to normal tissues of these NPs was also discovered, further demonstrating the safety and potential application of this small molecule in clinical practice.

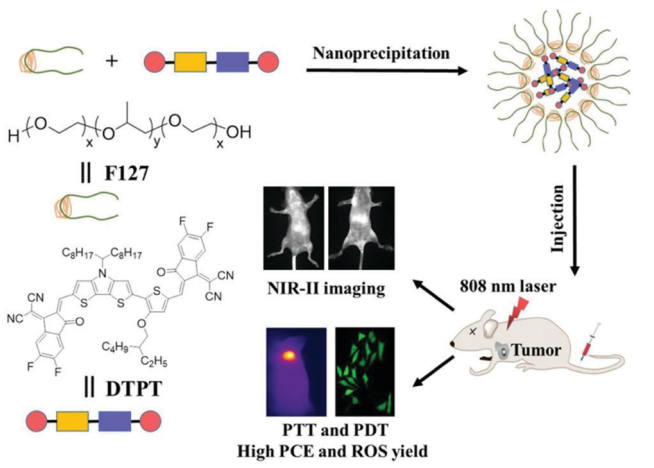

Scheme 1 Schematic of versatile nanoparticles for high performance tumor phototheranostics.

Results and discussion

Scheme S1 (ESI†) displays the synthetic route of small molecule DTPT. The structure of DTPT was demonstrated *via* NMR and MALDI-TOF MS (Fig. S1–S7, ESI†). Water-soluble DTPT NPs were easily acquired *via* a simple nanoprecipitation method using Pluronic F127 as an encapsulation matrix. The data from the TEM assay revealed that the DTPT NPs possess uniform spherical morphology with a diameter of about 90 nm (Fig. 1a), indicating the possible passive tumor-targeting capability of the NPs based on the enhanced permeability and retention effects. The average hydrodynamic size of DTPT NPs was also studied by DLS (Fig. 1a), which matched well with the TEM results. Besides, DTPT NPs displayed outstanding long-term stability with insignificant size change within 5 weeks (Fig. 1b). UV-Vis-NIR spectroscopy confirmed that DTPT NPs in water exhibit broad absorption over 650–900 nm (Fig. 1c), and the molar absorption coefficient at 808 nm of DTPT NPs was as high as 3.49×10^4 M^{-1} cm^{-1} (Fig. S8, ESI†), indicating their excellent 808 nm laser absorbance capability. As shown in Fig. 1d, in contrast with indocyanine green (ICG, an FDA-approved NIR dye), the absorption of DTPT NPs displayed negligible change under continuous 808 nm laser irradiation (60 min), suggesting the superb photostability of DTPT NPs. Moreover, DTPT NPs presented outstanding NIR-II fluorescence emission

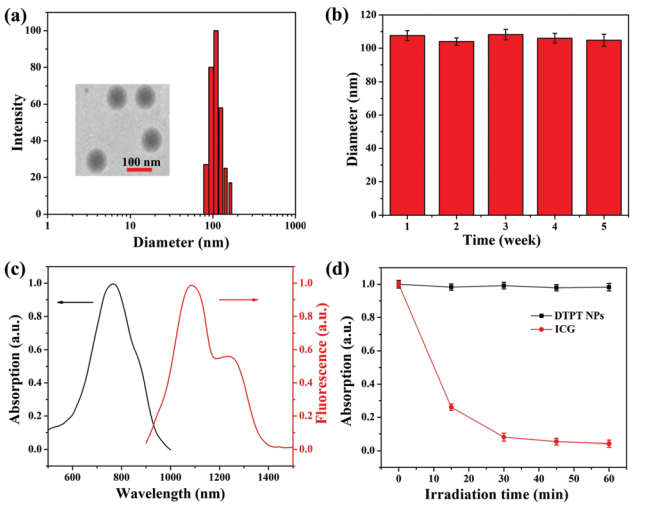

Fig. 1 DTPT NP characterizations. (a) TEM and DLS results. (b) Long-term stability test. (c) Normalized absorption and fluorescence spectra. (d) Photostability test.

(a major peak at 1087 nm and a shoulder peak at 1242 nm, Fig. 1c) with an appropriate quantum yield (0.76%, using IR-26 as a standard, Fig. S9, ESI†), which provides a suitable candidate for phototheranostics.

Owing to the gratifying optical absorbance capability, the photothermal performances of DTPT NPs were attentively tested. Fig. 2a shows the photothermal profiles of DTPT NPs with various concentrations. Upon 808 nm laser illumination (1 W cm^{-2}), higher resultant temperatures of DTPT NPs were found as the concentrations increased, suggesting an apparent concentration-dependent heating effects. When the concentration was 100 μg mL^{-1}, the temperature of the dispersion solution rose quickly to 46.5 °C in 3 min and reached up to 53.1 °C in 10 min, which was enough for efficaciously and irreversibly ablating the tumor cells. Nevertheless, under identical conditions, the temperature change of pure water is inappreciable, corroborating the outstanding photo-to-thermal conversion ability of DTPT NPs. The infrared thermal images of all solutions are presented in Fig. 2b, which further demonstrated the temperature changes. Then, DTPT NPs (100 μg mL^{-1}) were illuminated by an 808 nm laser with diverse power densities. As shown in Fig. 2c, it was distinctly observed that the temperature rise of the DTPT NP solution was positively correlated with the density of the laser. Photothermal stability, as a crucial parameter for tumor therapy, was next studied to evaluate the performance of DTPT NPs. Fig. 2d shows that no apparent difference of temperature elevation upon 808 nm laser illumination for four on/off cycles, affirming their gratifying photothermal stability. As another important parameter to evaluate the performance of DTPT NPs, the PCE value of DTPT NPs was measured based on one on/off cycle. The PCE value was calculated to be as high as 61.6% (Fig. S10, ESI†), which is more extraordinary than that of numerous small molecule nanoparticles,[22] conjugated polymer nanoparticles,[23] and inorganic nanoparticles.[24]

Next, the photodynamic performances of DTPT NPs were investigated upon 808 nm laser irradiation, in which 1,3-diphenylisobenzofuran (DPBF) and indocyanine green (ICG) were used as the singlet oxygen ($^1O_2$) probe and comparison standard, respectively. The absorption spectra of DPBF treated with DTPT NPs upon 808 nm irradiation are depicted in Fig. S11 (ESI†). It can be seen that the DPBF absorption declined largely upon increasing the power density, confirming $^1O_2$ generation in these NPs. In particular, compared to ICG, DTPT NPs exhibited a larger DPBF degradation rate (~7.1 times of ICG, Fig. 3a–c). Besides, the intracellular ROS generation of DTPT NPs upon 808 nm irradiation was tested using 2′,7′-dichlorodihydrofluorescein diacetate as a detection probe (Fig. 3d). In DTPT NPs + laser group, bright green fluorescence was found. In the DTPT NPs without the laser group, insignificant fluorescence was found, affirming the outstanding NIR-induced $^1O_2$ production of DTPT NPs in cells. All these conclusions displayed that DTPT NPs can be used as a promising nanoplatform for PTT/PDT combination therapy.

Excellent biocompatibility of nanomaterials is an essential prerequisite for biomedical applications. The cell viabilities of NIH-3T3 normal cells after incubation with DTPT NPs were estimated by MTT assays. Fig. 4a affirms that DTPT NPs showed inappreciable cytotoxicity even at a high concentration (200 μg mL^{-1}), displaying their exceedingly good biocompatibility. *In vitro* therapeutic efficacy of DTPT NPs was further estimated by MTT assays. As shown in Fig. 4b, the HeLa cells cultivated with DTPT NPs in different concentrations retained remarkable survival rates without the 808 nm laser illumination, suggesting no dark toxicity of DTPT NPs to cells. However, in the DTPT NPs with the 808 nm laser illumination group, the survival rates of HeLa cells were reduced as the concentrations of DTPT NPs increased, which was due to the excellent PTT/PDT performances of DTPT NPs. Live and dead cell viability assays were further investigated to visually appraise

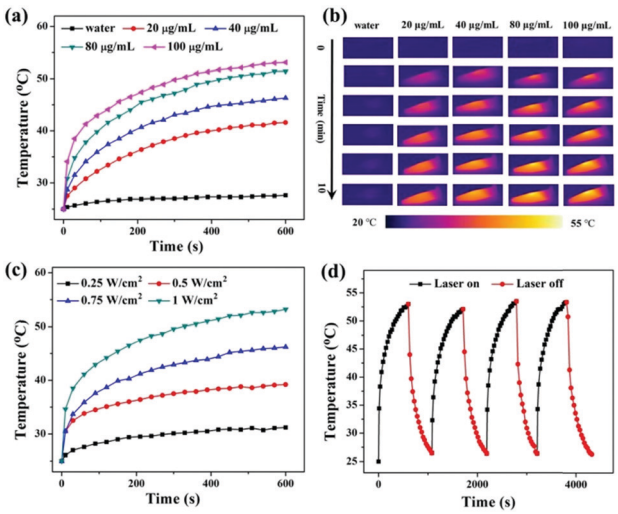

Fig. 2 (a) Photothermal profiles of DTPT NPs with various concentrations. (b) Infrared thermal images of all solutions. (c) Photothermal profiles of DTPT NPs with diverse power densities. (d) Photothermal stability test of DTPT NPs (100 μg mL^{-1}).

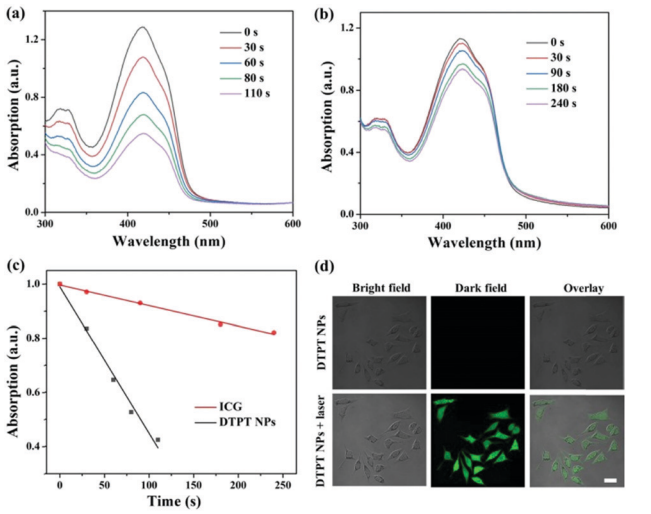

Fig. 3 Absorption spectra of DPBF treated with (a) DTPT NPs and (b) ICG upon 808 nm irradiation. (c) Degradation rate of DPBF absorbance treated with DTPT NPs and ICG, respectively. (d) Measurement of ROS generation in cells (scale bar: 20 μm).

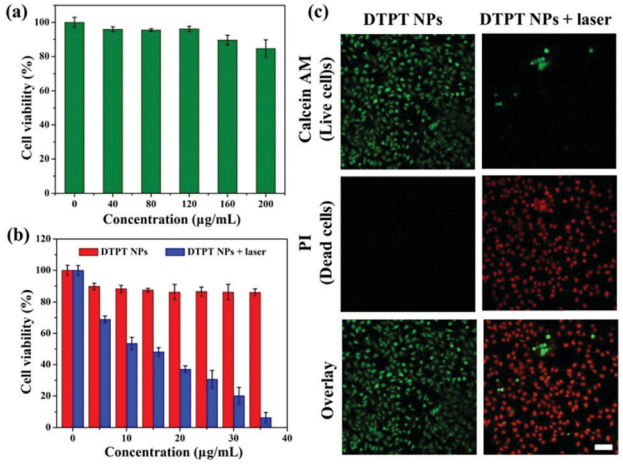

Fig. 4 (a) Biocompatibility estimation of DTPT NPs. *In vitro* therapeutic efficacy of DTPT NPs estimated using (b) MTT and (c) live/dead assays (scale bar: 20 μm).

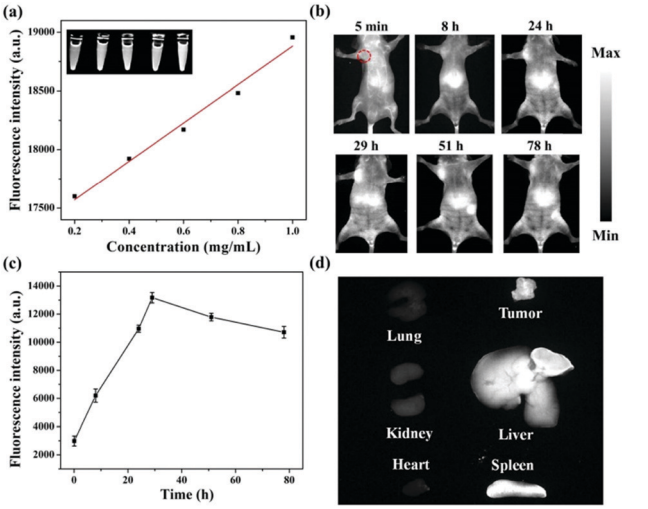

Fig. 5 (a) NIR-II imaging property of DTPT NPs *in vitro*. NIR-II (b) images and (c) signals of DTPT NPs *in vivo*. (d) NIR-II images of excised organs and tumor.

the therapeutic efficacy, in which live and dead cells are shown in green fluorescence (calcein-AM) and red fluorescence (propidium iodide, PI), respectively. Fig. 4c demonstrates that only green fluorescence was found in the DTPT NP group, further implying no dark toxicity of DTPT NPs to cells. Nevertheless, broad red fluorescence was found upon 808 nm laser illumination, suggesting the outstanding phototoxicity of DTPT NPs. All these data indicate that DTPT NPs possess good biocompatibility, inappreciable dark toxicity, and prominent phototoxicity and can serve as promising phototherapeutic agents *in vivo*.

Imaging plays an essential role in tumor treatment, which has the ability to confirm the optimal therapeutic time, tumor location, and real-time monitoring of the treatment outcome. Before imaging, the blood metabolism of NPs was first studied, which showed a single-compartment pharmacokinetic model (Fig. S12, ESI†). Then, the NIR-II fluorescence imaging property of DTPT NPs *in vitro* was investigated. The NIR-II signal values and the brightness of NIR-II images were both markedly raised with the rise of the concentration of DTPT NPs (Fig. 5a). Moreover, the NIR-II signals of DTPT NPs (1 mg mL^{-1}) could still be detected even when covered with 10 mm of a chicken-breast tissue, making DTPT NPs hopeful bioimaging agents with deep tissue penetration (Fig. S13, ESI†). The NIR-II imaging property of DTPT NPs *in vivo* was studied using a HeLa subcutaneous xenograft tumor mouse model by the tail intravenous injection of NPs. As presented in the *in vivo* NIR-II images (Fig. 5b), the whole-body vessels are clearly discerned from the surrounding background tissues after injection immediately, which was difficult to achieve using traditional NIR-I fluorescence imaging. In addition, the tumor region exhibited gradually enhanced NIR-II fluorescence signals, indicating the gratifying tumor accumulation and fluorescence lighting abilities of the NPs. It should be noted that the NIR-II signals appeared after maximum 29 h of injection (tumour-to-normal-tissue ratio: 1.86) and decreased gradually afterwards owing to metabolism (Fig. 5c). Therefore, 29 h post-injection was determined as an optimal therapeutic time *in vivo*. Besides, appreciable NIR-II signals are still observed in the tumor region even after 78 h of injection, suggesting the long retention time and long imaging time of DTPT NPs *in vivo*. Moreover, the NPs showed a higher accumulation in the tumor, liver, and spleen than in heart, lungs, and kidneys, which is affirmed by the NIR-II fluorescence images and fluorescence semi-quantitation of excised tumor and organs (Fig. 5d and Fig. S14, ESI†). All these discoveries corroborated that DTPT NPs could provide powerful guidance for tumor theranostics.

Encouraged by the excellent *in vitro* therapeutic efficacy of DTPT NPs, the capability of DTPT NPs to produce hyperthermia *in vivo* was first tested. After 29 h of tail intravenous injection, the temperatures of the tumor were monitored upon the 808 nm laser illumination. As shown in Fig. 6a and Fig. S15 (ESI†), the change in temperature in the PBS group was inappreciable, while the temperature of the tumor in the DTPT NPs group increased to 55 °C after 2 min laser illumination, providing ample hyperthermia for the destruction of cancer cells. Subsequently, four groups of mice were given different treatments to evaluate the *in vivo* phototherapeutic effects of DTPT NPs by monitoring the changes in the tumor volume (Fig. 6b–d). Similar to control groups, the DTPT NP injected mice exhibited high tumor growth rates, manifesting inappreciable antitumor effects of DTPT NPs in dark. The tumor growth rates of mice treated with DTPT NPs and 808 nm laser irradiation were inhibited significantly due to the outstanding PTT/PDT effects of DTPT NPs (90.8% tumor inhibition rate). The changes in the tumor weight were also monitored, which also corroborated the outstanding phototherapeutic effects of DTPT NPs (Fig. 6e). Moreover, the fluctuations in the body weights of mice were studied to assess the side effects of DTPT NPs. As presented in Fig. 6f, the same trend in the body weight changes in all groups was found, indicating inappreciable harm of DTPT NPs *in vivo*.

The biosafety of DTPT NPs was further appraised by hematoxylin and eosin (H&E) staining. As presented in Fig. 7, no abnormalities were found in these major organs. However, astonishing lesions

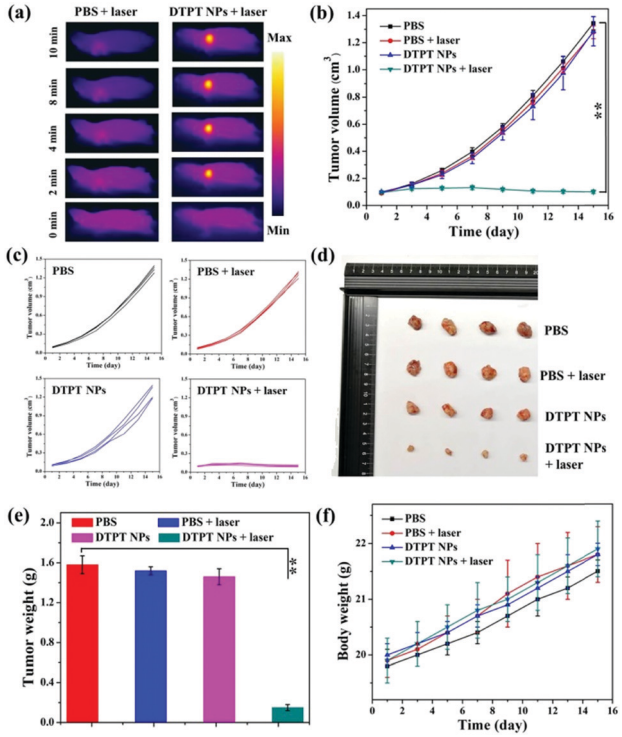

Fig. 6 (a) Thermal imaging of tumor under laser illumination. (b) Changes in tumor volume during therapy. (c) Tumor growth curves during therapy. (d) Tumor photos after therapy. (e) Changes in the tumor weight during therapy. (f) Changes in the body weights of mice during therapy. $^{**}P < 0.01$ (one-way ANOVA).

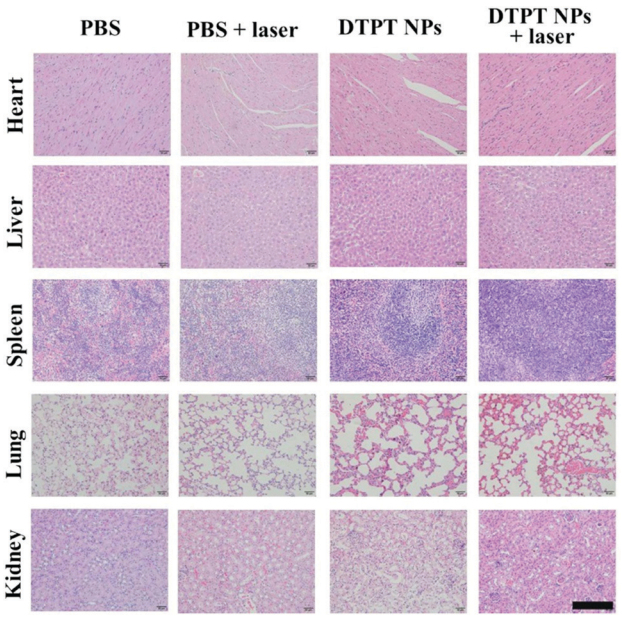

Fig. 7 Organ sections from each group (scale bar: 200 μm).

were evidently discovered in these tumors handled with DTPT NPs and illumination (Fig. S16, ESI†), revealing the superb safety towards normal tissues and astounding harm to tumor tissues.

Conclusions

In summary, a novel nanoplatform based on single-component asymmetric small organic molecules was successfully constructed for high performance phototheranostics. Apart from the reported advantages of small molecule-based NPs, such as outstanding water-solubility, superb long-term stability, and preeminent photostability, the developed DTPT NPs possessed strong absorption at 808 nm, excellent NIR-II fluorescence emission, high hyperthermia (PCE was as high as 61.6%), and ROS generation ability. The results from *in vitro* and *in vivo* assays affirmed that the versatile DTPT NPs displayed significant antitumor efficacy under a single 808 nm laser irradiation (90.8% tumor inhibition rate), profiting from the satisfactory NIR-II fluorescence imaging and PTT/PDT performances. Moreover, these NPs showed superb safety to normal tissues, further demonstrating the potential application of this nanoagent in clinical practice. This study offers fundamental insights for the construction of small molecule-based nanoplatforms for high performance tumor theranostics.

Experimental section

Materials

F127 was obtained from Shanghai Yare Biotech, Inc. All starting materials used in the synthesis of DTPT were purchased from Sigma-Aldrich. Calcein AM/PI stain kit, NIH-3T3 cells, HeLa cells, and HeLa tumor-bearing mice were purchased from Jiangsu KeyGEN BioTECH Corp., Ltd.

Synthetic procedures

Detailed synthetic route of DTPT is presented in Scheme S1 (ESI†).

Synthesis of compound 2. Compound **1** (3.0 g, 7.2 mmol) in anhydrous THF (80 mL) was placed at −45 °C under nitrogen for 10 min, and *n*-BuLi (3.0 mL, 7.2 mmol) was added slowly. After stirring for 1.5 h, *N*,*N*-dimethylformamide (1.1 g, 14.4 mmol) was added. The solution was further stirred for 1 h at room temperature. After extraction and washing, the solvent was evaporated, and compound **2** could be obtained *via* column chromatography as a yellow solid (3.0 g, 93%). ^{1}H NMR (500 MHz, $CDCl_3$, δ): 9.88 (s, 1H), 7.67 (s, 1H), 7.36 (d, 1H), 7.03 (d, 1H), 4.25 (m, 1H), 2.02 (m, 2H), 1.86 (m, 2H), 1.25–1.14 (m, 22H), 1.08–1.00 (m, 2H), 0.84 (m, 6H). ^{13}C NMR (125 MHz, $CDCl_3$, δ): 183.20, 148.68, 143.56, 140.12, 128.46, 123.68, 120.35, 115.30, 111.85, 60.41, 35.29, 31.95, 29.47, 29.40, 29.32, 26.74, 22.80, 14.27.

Synthesis of compound 3. *N*-Methylpiperazine (858.6 mL, 7.7 mmol) in anhydrous THF (80 mL) was placed at −78 °C under nitrogen for 10 min, and then *n*-BuLi (3.2 mL, 7.7 mmol) was added slowly. After stirring for 30 min, compound 2 (3 g, 6.7 mmol) was added. After further stirring for 30 min, *n*-BuLi (3.2 mL, 7.7 mmol) was added. After stirring for 2 h at −20 °C, Bu_3SnCl (2.2 mL, 8.1 mmol) in anhydrous THF (3 mL) was added slowly at −78 °C. The solution was further stirred for 2 h at room temperature. Then, HCl (50 mL) was added at 0 °C for 2 min and neutralized with the Na_2CO_3 solution. After extraction and washing, the solvent was evaporated, and a viscous liquid

was obtained and directly used in the following step without further purification.

Synthesis of DTPT-CHO. Compound **3** (1.2 g, 1.6 mmol), compound **4** (625.7 mg, 2.0 mmol), and $Pd(PPh_3)_4$ (37.8 mg, 32.7 μmol) were added to anhydrous toluene (12 mL). The solution was stirred for 6 h at 110 °C under nitrogen, and the solvent was evaporated. DTPT-CHO could be obtained *via* column chromatography as an orange viscous liquid (950 mg, 85%). ^{1}H NMR (500 MHz, $CDCl_3$, δ): 9.87 (s, 1H), 9.77 (s, 1H), 7.65 (s, 1H), 7.50 (s, 1H), 7.44 (s, 1H), 4.24 (m, 1H), 4.16–4.10 (m, 2H), 2.02 (m, 2H), 1.88 (m, 3H), 1.60 (m, 4H), 1.40–1.32 (m, 4H), 1.23–1.13 (m, 22H), 1.06 (m, 2H), 0.99 (m, 3H), 0.92 (m, 3H), 0.80 (m, 6H). ^{13}C NMR (125 MHz, $CDCl_3$, δ): 182.98, 181.81, 154.08, 147.99, 144.24, 140.93, 136.74, 136.68, 129.09, 126.71, 123.50, 123.32, 116.27, 109.29, 74.46, 60.49, 39.93, 35.18, 31.88, 30.73, 29.42, 29.34, 29.27, 29.26, 26.73, 24.16, 23.19, 22.73, 14.25, 14.18, 11.36.

Synthesis of DTPT. Compound DTPT-CHO (200 mg, 292 μmol), 1,2-dichloroethane (20 mL), β-alanine (2.6 mg, 29.2 μmol), EtOH (4 mL), and 2-(5,6-difluoro-3-oxo-2,3-dihydro-1*H*-inden-1-ylidene) malononitrile (269 mg, 1.2 mmol) were mixed and stirred at 55 °C. Then, the solvent was evaporated. DTPT could be obtained *via* column chromatography as a dark-blue solid (250 mg, 77%). ^{1}H NMR (500 MHz, $CDCl_3$, δ): 8.87 (s, 1H), 8.73 (s, 1H), 8.51 (m, 2H), 7.79–7.63 (m, 3H), 7.54 (d, 2H), 4.30–4.18 (m, 3H), 2.07 (m, 2H), 1.94 (m, 3H), 1.67 (m, 4H), 1.45–1.38 (m, 4H), 1.30–1.17 (m, 22H), 1.12 (m, 2H), 1.05 (m, 3H), 0.96 (m, 3H), 0.81 (m, 6H). ^{13}C NMR (125 MHz, $CDCl_3$, δ): 186.30, 185.90, 158.52, 158.50, 157.78, 157.77, 157.75, 156.10, 153.44, 140.66, 138.50, 137.93, 136.99, 136.97, 136.91, 136.74, 136.71, 136.67, 136.34, 134.87, 134.64, 134.62, 134.61, 134.58, 133.35, 129.82, 125.97, 122.55, 120.45, 119.82, 115.36, 115.19, 114.98, 114.92, 114.83, 114.37, 114.33, 112.86, 112.70, 112.54, 110.12, 75.15, 70.42, 68.07, 61.25, 40.03, 35.12, 31.98, 30.75, 29.61, 29.52, 29.37, 29.36, 27.08, 24.30, 23.28, 22.82, 14.35, 14.26, 11.49. MALDI-TOF MS (*m*/*z*): $[M + H]^+$ calcd for $C_{34}H_{35}NO_4S_4$, 1107.3873; found, 1107.3861.

Preparation of DTPT NPs

DTPT (1 mg) and F127 (10 mg) were dissolved in THF. Then, the solution was quickly injected into water under sonication. Then, DTPT NPs were obtained after centrifugation.

Evaluation of the photothermal/photodynamic performances of NPs

For photothermal performance, the various concentrations of DTPT NPs were exposed to an 808 nm laser (1 W cm^{-2}). Besides, 100 μg mL^{-1} DTPT NPs was exposed to an 808 nm laser with different power densities. The temperature changes and real-time thermal imaging of DTPT NPs were recorded using an infrared thermal imaging camera. For photodynamic performance, the mixture of ROS probe and DTPT NPs were exposed to an 808 nm laser with different power densities. The absorption of the probe was recorded using a UV-Vis-NIR spectrophotometer.

MTT assay

After 24 h of NIH-3T3 or HeLa cells cultivation in the DMEM medium with 10% FBS, various concentrations of DTPT NPs were co-cultured with the NIH-3T3 or HeLa cells for another 24 or 4 h. Moreover, one group of HeLa cells was treated without laser illumination. Another group was treated with 808 nm laser (1 W cm^{-2}, 4 min) illumination. After further culture of cells with a fresh culture medium, an MTT assay was carried out. The absorbance was determined with a microplate reader.

In vivo NIR-II imaging

The imaging performance of DTPT NPs was tested using HeLa subcutaneous xenograft tumor mouse model. After injection of NPs (2 mg mL^{-1}, 150 μL), NIR-II images were acquired utilizing an *in vivo* NIR-II imaging system (E_x = 808 nm).

In vivo cancer treatment

All animal investigations were studied with the permit from the Animal Ethics Committee of Simcere BioTech Corp., Ltd., and performed in accordance with the Guidelines for Care and Use of Laboratory Animals of Jiangsu KeyGEN BioTECH Corp., Ltd (china). Four groups (4 mice each) of mice were given different treatments: (1) PBS (150 μL), (2) PBS (150 μL) and 808 nm laser irradiation (1 W cm^{-2}, 10 min), (3) DTPT NPs (1 mg mL^{-1}, 150 μL), (4) DTPT NPs (1 mg mL^{-1}, 150 μL) and 808 nm laser (1 W cm^{-2}, 10 min). After tail intravenous injection, the changes in tumor volume, tumor weight, and mice body weight were monitored to evaluate the *in vivo* treatment effect of DTPT NPs. H&E staining of major organs and tumor was carried out after treatment using standard techniques for histology studies.

Conflicts of interest

There are no conflicts to declare.

Acknowledgements

This work was supported by the National Natural Science Foundation of China (No. 21602112, 21674048), the Macao Young Scholars Program (No. AM2020030), NUPTSF (No. NY220198), the Open Research Fund of State Key Laboratory of Bioelectronics, Southeast University (No. OPSKLB202006).

Notes and references

1 (*a*) X. Wan, L. Song, W. Pan, H. Zhong, N. Li and B. Tang, Tumor-targeted cascade nanoreactor based on metal–organic frameworks for synergistic ferroptosis–starvation anticancer therapy, *ACS Nano*, 2020, **14**, 11017–11028; (*b*) M. Chen, X. Zhou, R. Chen, J. Wang, R. D. Ye, Y. Wang, C. Wu and R. I. Mahato, Nano-carriers for delivery and targeting of active ingredients of Chinese medicine for hepatocellular carcinoma therapy, *Mater. Today*, 2019, **25**, 66–87; (*c*) H.-J. Yoon, H.-S. Lee, J.-H. Jung, H. K. Kim and J.-H. Park, Photothermally amplified therapeutic liposomes for effective combination

treatment of cancer, *ACS Appl. Mater. Interfaces*, 2018, **10**, 6118–6123.

2 (*a*) Z. Yang and X. Chen, Semiconducting perylene diimide nanostructure: Multifunctional phototheranostic nanoplatform, *Acc. Chem. Res.*, 2019, **52**, 1245–1254; (*b*) J. Zhang, L. Ning, J. Huang, C. Zhang and K. Pu, Activatable molecular agents for cancer theranostics, *Chem. Sci.*, 2020, **11**, 618–630; (*c*) X. Lu, J. Chen, J. Li, B. Xia, J. Xu, Q. Wang, C. Xie, Q. Fan and W. Huang, Single nanoparticles as versatile phototheranostics for tri-modal imaging-guided photothermal therapy, *Biomater. Sci.*, 2019, **7**, 3609–3613; (*d*) Q. Wang, J. Cai, X. Niu, J. Wang, J.-W. Liu, C. Xie, W. Huang and Q. Fan, Rational design of high performance nanotheranostics for NIR-II fluorescence/magnetic resonance imaging guided enhanced phototherapy, *Biomater. Sci.*, 2021, **9**, 3499–3506.

3 (*a*) Y. Cai, P. Liang, Q. Tang, X. Yang, W. Si, W. Huang, Q. Zhang and X. Dong, Diketopyrrolopyrrole–triphenylamine organic nanoparticles as multifunctional reagents for photoacoustic imaging-guided photodynamic/photothermal synergistic tumor therapy, *ACS Nano*, 2017, **11**, 1054–1063; (*b*) Y. Ma, J. Huang, S. Song, H. Chen and Z. Zhang, Cancer-targeted nanotheranostics: Recent advances and perspectives, *Small*, 2016, **12**, 4936–4954; (*c*) G. Feng and B. Liu, Multifunctional AIEgens for future theranostics, *Small*, 2016, **12**, 6528–6535; (*d*) D. Zheng, P. Yu, Z. Wei, C. Zhong, M. Wu and X. Liu, RBC membrane camouflaged semiconducting polymer nanoparticles for near-infrared photoacoustic imaging and photothermal therapy, *Nano-Micro Lett.*, 2020, **12**, 94.

4 (*a*) B. Qiao, Y. Luo, H.-B. Cheng, J. Ren, J. Cao, C. Yang, B. Liang, A. Yang, X. Yuan, J. Li, L. Deng, P. Li, H.-T. Ran, L. Hao, Z. Zhou, M. Li, Y. Zhang, P. S. Timashev, X.-J. Liang and Z. Wang, Artificial nanotargeted cells with stable photothermal performance for multimodal imaging-guided tumor-specific therapy, *ACS Nano*, 2020, **14**, 12652–12667; (*b*) Q. Wang, J. Xu, R. Geng, J. Cai, J. Li, C. Xie, W. Tang, Q. Shen, W. Huang and Q. Fan, High performance one-for-all phototheranostics: NIR-II fluorescence imaging guided mitochondria-targeting phototherapy with a single-dose injection and 808 nm laser irradiation, *Biomaterials*, 2020, **231**, 119671; (*c*) Q. Wang, L. Tian, J. Xu, B. Xia, J. Li, F. Lu, X. Lu, W. Wang, W. Huang and Q. Fan, Multifunctional supramolecular vesicles for combined photothermal/photodynamic/hypoxia-activated chemotherapy, *Chem. Commun.*, 2018, **54**, 10328–10331.

5 (*a*) F. Xu, H. Li, Q. Yao, H. Ge, J. Fan, W. Sun, J. Wang and X. Peng, Hypoxia-activated NIR photosensitizer anchoring in the mitochondria for photodynamic therapy, *Chem. Sci.*, 2019, **10**, 10586–10594; (*b*) X. Gao, S. Jiang, C. Li, Y. Chen, Y. Zhang, P. Huang and J. Lin, Highly photostable croconium dye-anchored cell membrane vesicle for tumor pH-responsive duplex imaging-guided photothermal therapy, *Biomaterials*, 2021, **267**, 120454; (*c*) J. Huang and K. Pu, Near-infrared fluorescent molecular probes for imaging and diagnosis of nephro-urological diseases, *Chem. Sci.*, 2021, **12**, 3379–3392.

6 F. Ding, Y. Zhan, X. Lu and Y. Sun, Recent advances in near-infrared II fluorophores for multifunctional biomedical imaging, *Chem. Sci.*, 2018, **9**, 4370–4380.

7 (*a*) H. S. Jung, P. Verwilst, A. Sharma, J. Shin, J. L. Sessler and J. S. Kim, Organic molecule-based photothermal agents: An expanding photothermal therapy universe, *Chem. Soc. Rev.*, 2018, **47**, 2280–2297; (*b*) J. Zou, Z. Yin, P. Wang, D. Chen, J. Shao, Q. Zhang, L. Sun, W. Huang and X. Dong, Photosensitizer synergistic effects: D–A–D structured organic molecule with enhanced fluorescence and singlet oxygen quantum yield for photodynamic therapy, *Chem. Sci.*, 2018, **9**, 2188–2194; (*c*) D. Xi, M. Xiao, J. Cao, L. Zhao, N. Xu, S. Long, J. Fan, K. Shao, W. Sun, X. Yan and X. Peng, NIR light-driving barrier-free group rotation in nanoparticles with an 88.3% photothermal conversion efficiency for photothermal therapy, *Adv. Mater.*, 2020, **32**, 1907855; (*d*) Y. Wan, G. Lu, W.-C. Wei, Y.-H. Huang, S. Li, J.-X. Chen, X. Cui, Y.-F. Xiao, X. Li, Y. Liu, X.-M. Meng, P. Wang, H.-Y. Xie, J. Zhang, K.-T. Wong and C.-S. Lee, Stable organic photosensitizer nanoparticles with absorption peak beyond 800 nanometers and high reactive oxygen species yield for multimodality phototheranostics, *ACS Nano*, 2020, **14**, 9917–9928; (*e*) S. Liu, X. Zhou, H. Zhang, H. Ou, J. W. Y. Lam, Y. Liu, L. Shi, D. Ding and B. Z. Tang, Molecular motion in aggregates: Manipulating TICT for boosting photothermal theranostics, *J. Am. Chem. Soc.*, 2019, **141**, 5359–5368; (*f*) W. Shao, C. Yang, F. Li, J. Wu, N. Wang, Q. Ding, J. Gao and D. Ling, Molecular design of conjugated small molecule nanoparticles for synergistically enhanced PTT/PDT, *Nano-Micro Lett.*, 2020, **12**, 147.

8 (*a*) P. T. Sujai, M. M. Joseph, V. Karunakaran, G. Saranya, R. N. Adukkadan, S. Shamjith, R. Thomas, J. B. Nair, R. S. Swathi and K. K. Maiti, Biogenic cluster-encased gold nanorods as a targeted three-in-one theranostic nanoenvelope for SERS-guided photochemotherapy against metastatic melanoma, *ACS Appl. Bio Mater.*, 2018, **2**, 588–600; (*b*) X. Li, F. Fang, B. Sun, C. Yin, J. Tan, Y. Wan, J. Zhang, P. Sun, Q. Fan, P. Wang, S. Li and C. S. Lee, Near-infrared small molecule coupled with rigidness and flexibility for high-performance multimodal imaging-guided photodynamic and photothermal synergistic therapy, *Nanoscale Horiz.*, 2021, **6**, 177–185; (*c*) J. Li, X. Ni, J. Zhang, Y. Liang, Z. Gao, X. Zhang, D. Zheng and D. Ding, A fluorescence and photoactivity dual-activatable prodrug with self-synergistic magnification of the anticancer effect, *Mater. Chem. Front.*, 2019, **3**, 1349–1356; (*d*) Q. Wang, Y. Dai, J. Xu, J. Cai, X. Niu, L. Zhang, R. Chen, Q. Shen, W. Huang and Q. Fan, All-in-one phototheranostics: Single laser triggers NIR-II fluorescence/photoacoustic imaging guided photothermal/photodynamic/chemo combination therapy, *Adv. Funct. Mater.*, 2019, **29**, 1901480.

9 C. Li, G. Chen, Y. Zhang, F. Wu and Q. Wang, Advanced fluorescence imaging technology in the near-infrared-II window for biomedical applications, *J. Am. Chem. Soc.*, 2020, **142**, 14789–14804.

10 (*a*) X. Zhu, C. Liu, Z. Hu, H. Liu, J. Wang, Y. Wang, X. Wang, R. Ma, X. Zhang, H. Sun and Y. Liang, High brightness

NIR-II nanofluorophores based on fused-ring acceptor molecules, *Nano Res.*, 2020, **13**, 2570–2575; (*b*) Y. Li, D. Hu, Z. Sheng, T. Min, M. Zha, J.-S. Ni, H. Zheng and K. Li, Self-assembled AIEgen nanoparticles for multiscale NIR-II vascular imaging, *Biomaterials*, 2021, **264**, 120365; (*c*) S. Zhu, R. Tian, A. L. Antaris, X. Chen and H. Dai, Near-infrared-II molecular dyes for cancer imaging and surgery, *Adv. Mater.*, 2019, **31**, 1900321.

11 (*a*) M. Zhao, R. Wang, B. Li, Y. Fan, Y. Wu, X. Zhu and F. Zhang, Precise *in vivo* inflammation imaging using *in situ* responsive cross-linking of glutathione-modified ultra-small NIR-II lanthanide nanoparticles, *Angew. Chem., Int. Ed.*, 2019, **58**, 2050–2054; (*b*) C. Song, Y. Zhang, C. Li, G. Chen, X. Kang and Q. Wang, Enhanced nanodrug delivery to solid tumors based on a tumor vasculature-targeted strategy, *Adv. Funct. Mater.*, 2016, **26**, 4192–4200; (*c*) Z. Ma, M. Zhang, J. Yue, C. Alcazar, Y. Zhong, T. C. Doyle, H. Dai and N. F. Huang, Near-infrared IIb fluorescence imaging of vascular regeneration with dynamic tissue perfusion measurement and high spatial resolution, *Adv. Funct. Mater.*, 2018, **28**, 1803417.

12 (*a*) S. Liu, C. Chen, Y. Li, H. Zhang, J. Liu, R. Wang, S. T. H. Wong, J. W. Y. Lam, D. Ding and B. Z. Tang, Constitutional isomerization enables bright NIR-II AIEgen for brain-inflammation imaging, *Adv. Funct. Mater.*, 2019, **30**, 1908125; (*b*) J. Lin, X. Zeng, Y. Xiao, L. Tang, J. Nong, Y. Liu, H. Zhou, B. Ding, F. Xu, H. Tong, Z. Deng and X. Hong, Novel near-infrared II aggregation-induced emission dots for *in vivo* bioimaging, *Chem. Sci.*, 2019, **10**, 1219–1226; (*c*) S. He, J. Song, J. Qu and Z. Cheng, Crucial breakthrough of second near-infrared biological window fluorophores: Design and synthesis toward multimodal imaging and theranostics, *Chem. Soc. Rev.*, 2018, **47**, 4258–4278.

13 F. Peng, M. I. Setyawati, J. K. Tee, X. Ding, J. Wang, M. E. Nga, H. K. Ho and D. T. Leong, Nanoparticles promote *in vivo* breast cancer cell intravasation and extravasation by inducing endothelial leakiness, *Nat. Nanotechnol.*, 2019, **14**, 279–286.

14 J. Chen, K. Wen, H. Chen, S. Jiang, X. Wu, L. Lv, A. Peng, S. Zhang and H. Huang, Achieving high-performance photothermal and photodynamic effects upon combining D–A structure and nonplanar conformation, *Small*, 2020, **16**, 2000909.

15 (*a*) Z. Sheng, B. Guo, D. Hu, S. Xu, W. Wu, W. H. Liew, K. Yao, J. Jiang, C. Liu, H. Zheng and B. Liu, Bright aggregation-induced-emission dots for targeted synergetic NIR-II fluorescence and NIR-I photoacoustic imaging of orthotopic brain tumors, *Adv. Mater.*, 2018, **30**, 1800766; (*b*) K. Shou, C. Qu, Y. Sun, H. Chen, S. Chen, L. Zhang, H. Xu, X. Hong, A. Yu and Z. Cheng, Multifunctional biomedical imaging in physiological and pathological conditions using a NIR-II probe, *Adv. Funct. Mater.*, 2017, **27**, 1700995; (*c*) A. L. Antaris, H. Chen, S. Diao, Z. Ma, Z. Zhang, S. Zhu, J. Wang, A. X. Lozano, Q. Fan, L. Chew, M. Zhu, K. Cheng, X. Hong, H. Dai and Z. Cheng, A high quantum yield molecule-protein complex fluorophore for near-infrared II imaging, *Nat. Commun.*, 2017, **8**, 15269; (*d*) R. Sang, X. Xu, Q. Wang, Q. Fan and W. Huang, Near-infrared-II fluorescence probes based on organic small molecules, *Acta Chim. Sin.*, 2020, **78**, 901–915.

16 (*a*) J. Qi, C. Sun, A. Zebibula, H. Zhang, R. T. K. Kwok, X. Zhao, W. Xi, J. W. Y. Lam, J. Qian and B. Z. Tang, Real-time and high-resolution bioimaging with bright aggregation-induced emission dots in short-wave infrared region, *Adv. Mater.*, 2018, **30**, 1706856; (*b*) G. Xu, Q. L. Yan, X. G. Lv, Y. Zhu, K. Xin, B. Shi, R. C. Wang, J. Chen, W. Gao, P. Shi, C. H. Fan, C. C. Zhao and H. Tian, Imaging of colorectal cancers using activatable nanoprobes with second near-infrared window emission, *Angew. Chem., Int. Ed.*, 2018, **57**, 3626–3630; (*c*) Q. Wang, B. Xia, J. Xu, X. Niu, J. Cai, Q. Shen, W. Wang, W. Huang and Q. Fan, Biocompatible small organic molecule phototheranostics for NIR-II fluorescence/photoacoustic imaging and simultaneous photodynamic/photothermal combination therapy, *Mater. Chem. Front.*, 2019, **3**, 650–655.

17 (*a*) R. Zhang, Y. Xu, Y. Zhang, H. S. Kim, A. Sharma, J. Gao, G. Yang, J. S. Kim and Y. Sun, Rational design of a multifunctional molecular dye for dual-modal NIR-II/photoacoustic imaging and photothermal therapy, *Chem. Sci.*, 2019, **10**, 8348–8353; (*b*) X. Zeng, Y. Xiao, J. Lin, S. Li, H. Zhou, J. Nong, G. Xu, H. Wang, F. Xu, J. Wu, Z. Deng and X. Hong, Near-infrared II dye–protein complex for biomedical imaging and imaging-guided photothermal therapy, *Adv. Healthcare Mater.*, 2018, **7**, 1800589; (*c*) R. Zhang, Z. Wang, L. Xu, Y. Xu, Y. Lin, Y. Zhang, Y. Sun and G. Yang, Rational design of a multifunctional molecular dye with single dose and laser for efficiency NIR-II fluorescence/photoacoustic imaging guided photothermal therapy, *Anal. Chem.*, 2019, **91**, 12476–12483; (*d*) S. Gao, G. Wei, S. Zhang, B. Zheng, J. Xu, G. Chen, M. Li, S. Song, W. Fu, Z. Xiao and W. Lu, Albumin tailoring fluorescence and photothermal conversion effect of near-infrared-II fluorophore with aggregation-induced emission characteristics, *Nat. Commun.*, 2019, **10**, 2206.

18 (*a*) X. Zhang, J. Tang, C. Li, Y. Lu, L. Cheng and J. Liu, A targeting black phosphorus nanoparticle based immune cells nano-regulator for photodynamic/photothermal and photo-immunotherapy, *Bioact. Mater.*, 2021, **6**, 472–489; (*b*) V. Priya, L. Cheng-Hong, V. Raviraj, C. Chi-Shiun and H. K. Chu, Designing multi-branched gold nanoechinus for NIR light activated dual modal photodynamic and photothermal therapy in the second biological window, *Adv. Mater.*, 2014, **26**, 6689–6695; (*c*) E.-K. Lim, T. Kim, S. Paik, S. Haam, Y.-M. Huh and K. Lee, Nanomaterials for theranostics: Recent advances and future challenges, *Chem. Rev.*, 2015, **115**, 327–394.

19 L. Yang, X. Song, J. Yu, H. Wang, Z. Zhang, R. Geng, J. Cao, D. Baran and W. Tang, Tuning of the conformation of asymmetric nonfullerene acceptors for efficient organic solar cells, *J. Mater. Chem. A*, 2019, **7**, 22279–22286.

20 Z. He, L. Zhao, Q. Zhang, M. Chang, C. Li, H. Zhang, Y. Lu and Y. Chen, An acceptor–donor–acceptor structured small molecule for effective NIR triggered dual phototherapy of cancer, *Adv. Funct. Mater.*, 2020, **30**, 1910301.

21 (*a*) G. Feng, G. Zhang and D. Ding, Design of superior phototheranostic agents guided by Jablonski diagrams,

Chem. Soc. Rev., 2020, **49**, 8179–8234; (*b*) J. Li, H. Gao, R. Liu, C. Chen, S. Zeng, Q. Liu and D. Ding, Endoplasmic reticulum targeted AIE bioprobe as a highly efficient inducer of immunogenic cell death, *Sci. China: Chem.*, 2020, **63**, 1428–1434.

22 (*a*) Z. Guo, Y. Zou, H. He, J. Rao, S. Ji, X. Cui, H. Ke, Y. Deng, H. Yang, C. Chen, Y. Zhao and H. Chen, Bifunctional platinated nanoparticles for photoinduced tumor ablation, *Adv. Mater.*, 2016, **28**, 10155–10164; (*b*) C. Ou, Y. Zhang, D. Pan, K. Ding, S. Zhang, W. Xu, W. Wang, W. Si, Z. Yang and X. Dong, Zinc porphyrin–polydopamine core–shell nanostructures for enhanced photodynamic/photothermal cancer therapy, *Mater. Chem. Front.*, 2019, **3**, 1786–1792; (*c*) C. Zhang, J. Wu, W. Liu, X. Zheng, W. Zhang, C.-S. Lee and P. Wang, Hypocrellin-based multifunctional phototheranostic agent for NIR-triggered targeted chemo/photodynamic/photothermal synergistic therapy against glioblastoma, *ACS Appl. Bio Mater*, 2020, **3**, 3817–3826.

23 (*a*) T. Sun, X. Chen, X. Wang, S. Liu, J. Liu and Z. Xie, Enhanced efficacy of photothermal therapy by combining a semiconducting polymer with an inhibitor of a heat shock protein, *Mater. Chem. Front.*, 2019, **3**, 127–136; (*b*) Y. X. Wang, L. H. Feng and S. Wang, Conjugated polymer nanoparticles for imaging, cell activity regulation, and therapy, *Adv. Funct. Mater.*, 2019, **29**, 1806818; (*c*) R.-H. Deng, M.-Z. Zou, D. Zheng, S.-Y. Peng, W. Liu, X.-F. Bai, H.-S. Chen, Y. Sun, P.-H. Zhou and X.-Z. Zhang, Nanoparticles from cuttlefish ink inhibit tumor growth by synergizing immunotherapy and photothermal therapy, *ACS Nano*, 2019, **13**, 8618–8629.

24 (*a*) W. Tang, W. Fan, W. Zhang, Z. Yang, L. Li, Z. Wang, Y. L. Chiang, Y. Liu, L. Deng, L. He, Z. Shen, O. Jacobson, M. A. Aronova, A. Jin, J. Xie and X. Chen, Wet/sono-chemical synthesis of enzymatic two-dimensional MnO2 nanosheets for synergistic catalysis-enhanced phototheranostics, *Adv. Mater.*, 2019, **31**, 1900401; (*b*) P. Wang, Y. Shi, S. Zhang, X. Huang, J. Zhang, Y. Zhang, W. Si and X. Dong, Hydrogen peroxide responsive iron–based nanoplatform for multimodal imaging–guided cancer therapy, *Small*, 2019, **15**, 1803791; (*c*) C. M. Hessel, V. P. Pattani, M. Rasch, M. G. Panthani, B. Koo, J. W. Tunnell and B. A. Korgel, Copper selenide nanocrystals for photothermal therapy, *Nano Lett.*, 2011, **11**, 2560–2566.